

Chevron-type graphene nanoribbons with a reduced energy band gap: Solution synthesis, scanning tunneling microscopy and electrical characterization

Ximeng Liu^{1,2,§}, Gang Li^{3,§}, Alexey Lipatov³, Tao Sun^{1,4}, Mohammad Mehdi Pour³, Narayana R. Aluru^{1,4}, Joseph W. Lyding^{1,2} (✉), and Alexander Sinitskii^{3,5} (✉)

¹ Beckman Institute for Advanced Science and Technology, University of Illinois at Urbana–Champaign, Urbana, IL 61801, USA

² Department of Electrical and Computer Engineering, University of Illinois at Urbana–Champaign, Urbana, IL 61801, USA

³ Department of Chemistry, University of Nebraska–Lincoln, Lincoln, NE 68588, USA

⁴ Department of Mechanical Science and Engineering, University of Illinois at Urbana–Champaign, Urbana, IL 61801, USA

⁵ Nebraska Center for Materials and Nanoscience, University of Nebraska–Lincoln, Lincoln, NE 68588, USA

[§] Ximeng Liu and Gang Li contributed equally to this work.

© Tsinghua University Press and Springer-Verlag GmbH Germany, part of Springer Nature 2020

Received: 12 January 2020 / Revised: 26 March 2020 / Accepted: 7 April 2020

ABSTRACT

Graphene nanoribbons (GNRs) attract a growing interest due to their tunable physical properties and promise for device applications. A variety of atomically precise GNRs have recently been synthesized by on-surface and solution approaches. While on-surface GNRs can be conveniently visualized by scanning tunneling microscopy (STM), and their electronic structure can be probed by scanning tunneling spectroscopy (STS), such characterization remains a great challenge for the solution-synthesized GNRs. Here, we report solution synthesis and detailed STM/STS characterization of atomically precise GNRs with a meandering shape that are structurally related to chevron GNRs but have a reduced energy band gap. The ribbons were synthesized by Ni⁰-mediated Yamamoto polymerization of specially designed molecular precursors using triflates as the leaving groups and oxidative cyclodehydrogenation of the resulting polymers using Scholl reaction. The ribbons were deposited onto III-V semiconducting InAs(110) substrates by a dry contact transfer technique. High-resolution STM/STS characterization not only confirmed the GNR geometry, but also revealed details of electronic structure including energy states, electronic band gap, as well as the spatial distribution of the local density of states. The experimental STS band gap of GNRs is about 2 eV, which is very close to 2.35 eV predicted by the density functional theory simulations with GW correction, indicating a weak screening effect of InAs(110) substrate. Furthermore, several aspects of GNR-InAs(110) substrate interactions were also probed and analyzed, including GNR tunable transparency, alignment to the substrate, and manipulations of GNR position by the STM tip. The weak interaction between the GNRs and the InAs(110) surface makes InAs(110) an ideal substrate for investigating the intrinsic properties of GNRs. Because of the reduced energy band gap of these ribbons, the GNR thin films exhibit appreciably high electrical conductivity and on/off ratios of about 10 in field-effect transistor measurements, suggesting their promise for device applications.

KEYWORDS

graphene nanoribbons, bottom-up synthesis, electronic structure, dry contact transfer, scanning tunneling microscopy, scanning tunneling spectroscopy

1 Introduction

Because of their tunable energy band gap, graphene nanoribbons (GNRs) are often viewed as promising materials for electronic applications [1–3]. Large quantities of GNRs with different structures can be produced by solution methods that involve Yamamoto [4–7], Suzuki-Miyaura [8–13] or Diels-Alder [14–17] polymerizations of specially designed monomers and planarization of the resulting polymers. However, although a considerable number of solution-synthesized GNRs have been reported over the last decade [18, 19], not many of them were electrically characterized or translated into electronic devices [7, 12, 20–23]. Several approaches were demonstrated for processing nanoscopic GNRs into macroscopically large structures, such

as films or fibrils, that are suitable for device fabrication and electrical measurements [20, 22, 24, 25]. However, a fundamental issue for the implementation of GNRs into electronic devices remains that many solution-synthesized nanoribbons intrinsically have large energy band gaps and thus are not expected to exhibit high conductivities and charge carrier mobilities.

This issue can be illustrated by the properties of chevron GNR, which was first synthesized by the on-surface polymerization of 6,11-dibromo-1,2,3,4-tetraphenyltriphenylene on Au(111) followed by the thermally induced cyclodehydrogenation [26]. The same monomer can be used to produce chevron GNRs in solution [5, 27], and the resulting ribbons can be self-assembled into uniform thin films for electrical measurements [22]. However, such films show very low electrical conductivities

Address correspondence to Joseph W. Lyding, lyding@illinois.edu; Alexander Sinitskii, sinitskii@unl.edu

due to the large energy band gap of the chevron GNR of about 3.7 eV, as predicted by first-principles calculations based on the GW approximation [7, 28–30]. When we previously designed laterally extended chevron GNRs [31], for which the GW simulations predicted a reduced band gap of 3.38 eV, these ribbons exhibited improved electrical conductivities in the form of self-assembled films compared to the original chevron GNRs [7]. Recently, Huang et al. reported another nanoribbon that has structural similarities with chevron GNR [6, 32, 33], see Fig. 1(a). This new ribbon also has a meandering structure and exactly the same width of about 1.7 nm as chevron GNR, if measured across the longitudinal axis of a nanoribbon (Scheme S2 in the Electronic Supplementary Material (ESM)), but less developed concave regions along the edges. Remarkably, these GNRs can be translated into thin-film field-effect transistors (FETs) with charge carrier mobilities of about $0.3 \text{ cm}^2 \cdot \text{V}^{-1} \cdot \text{s}^{-1}$ [6], which are higher than previously observed for structurally related ribbons. These promising results warrant theoretical and experimental investigations of the band gap of this new GNR, which have not been previously reported in literature.

Figure 1(b) shows the band structures of this GNR calculated using density functional theory (DFT) and GW approaches. The

GW simulations predict a band gap of $\Delta^{\text{GW}} = 2.35 \text{ eV}$, which is significantly smaller than the GW band gaps of chevron (3.7 eV) and extended chevron GNRs (3.38 eV) [7]. This band gap reduction is consistent with the improved device performance of these new nanoribbons [6]. This GW band gap is also smaller than that of the widely studied $N = 7$ armchair GNRs [26, 34] ($\Delta^{\text{GW}} = 3.7 \text{ eV}$) and comparable to $N = 9$ ($\Delta^{\text{GW}} = 2.1 \text{ eV}$) and $N = 13$ ($\Delta^{\text{GW}} = 2.35 \text{ eV}$) armchair GNRs [2], which were recently successfully employed in FETs with high on-currents and on/off ratios [35]. The DFT simulations, which are less computationally expensive than GW calculations but are known to underestimate band gaps of GNRs [2], predict a band gap of about 1 eV (Fig. 1(b)), which is also significantly smaller than similarly computed band gaps of chevron (1.6 eV) [26], extended chevron (1.38 eV) [7] and $N=7$ armchair GNRs (1.6 eV) [26].

For atomically precise GNRs that are directly grown on metal surfaces, such as Au(111), band gaps can be experimentally determined by scanning tunneling spectroscopy (STS) [34, 36–38]. It should be noted that the resulting STS band gaps are smaller than those predicted by GW simulations due to the substrate polarization effect [34]. For example, the experimental STS band gaps of chevron GNR ($\Delta^{\text{GW}} = 3.7 \text{ eV}$) on Au(111)

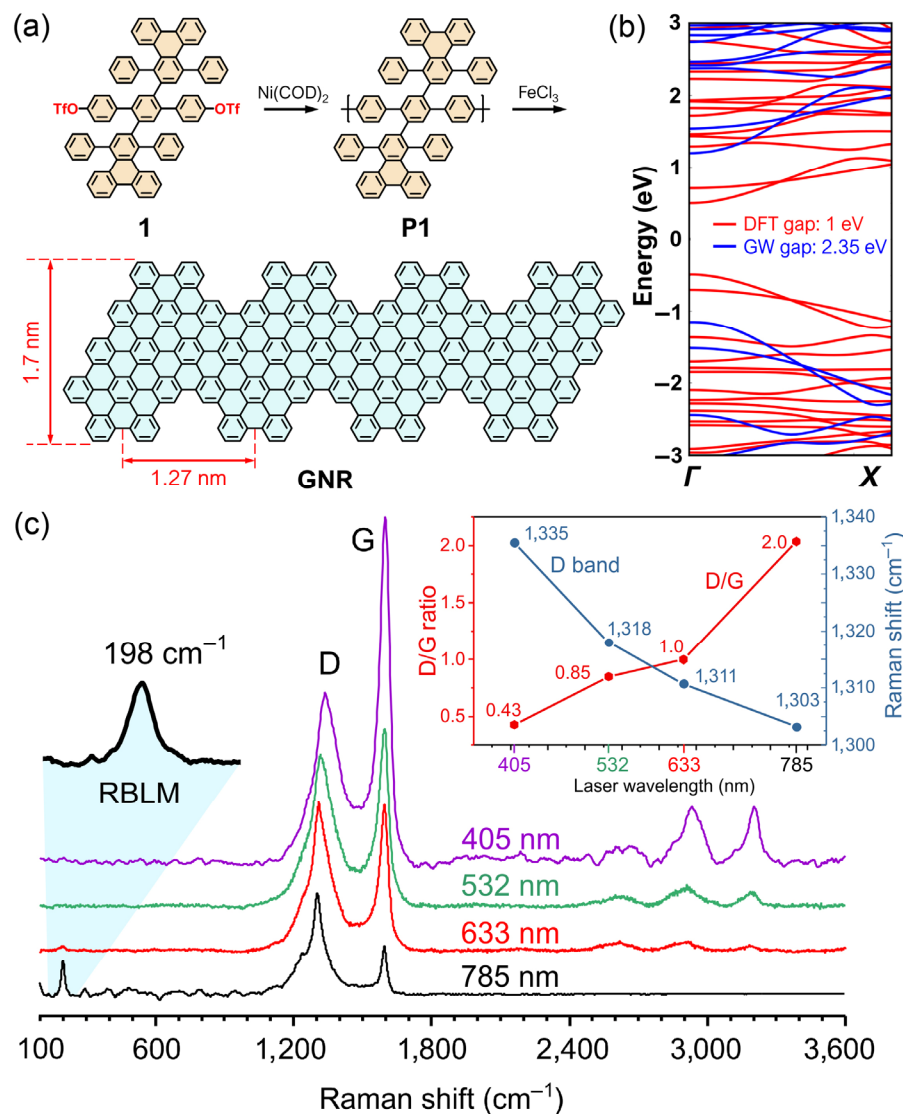


Figure 1 Solution synthesis of GNRs. (a) Scheme of the GNR synthesis. Triflate leaving groups in monomer 1 are highlighted in red. Polymerization: $\text{Ni}(\text{COD})_2$, 2,2'-bipyridine, 1,5-cyclooctadiene, dimethylformamide and toluene, 80 °C, 3 days, 89%. Cyclodehydrogenation: FeCl_3 , CH_3NO_2 , dichloromethane, 2 days, 90%. (b) DFT- and GW-calculated band structures of the GNR shown in panel (a). (c) Raman spectra of GNRs recorded using 405, 532, 633 and 785 nm excitation lasers. The inset shows the dependencies of the D band position and the D/G intensity ratio on the excitation laser wavelength.

are 2.4–2.53 eV [38–40]. However, STS characterization of solution-synthesized GNRs is more challenging, because the ribbons should be first transferred from ambient conditions to an ultrahigh vacuum (UHV) chamber of a scanning tunneling microscope, and the resulting sample should be free of solvent residues and other surface adsorbates. Recently, we demonstrated that this could be accomplished using the dry contact transfer (DCT) approach [7, 30]. In this method, a powder of solution-synthesized GNRs is first annealed in UHV conditions to remove residual solvent molecules and other adsorbates, and then, while still in a UHV chamber, pressed against a clean substrate for scanning tunneling microscopy (STM), which results in exfoliation of some ribbons to the substrate's surface. We previously used the DCT approach to deliver chevron and extended chevron GNRs to semiconductor substrates, such as H:Si(100) and InAs(110), and demonstrated adsorbate-free samples that were suitable for STS characterization [7, 30]. Importantly, on semiconductor substrates the band gap reduction due to the polarization effect should not be as large as on metal substrates, such as Au(111), and, for example, the STS measurements of chevron GNRs on H:Si(100) yielded a band gap of about 2.8 eV [30].

The primary goal of this study was to perform STM and STS characterization of these new chevron-family GNRs (Fig. 1(a)) with a reduced energy band gap. Our previous STM/STS studies of the solution-synthesized GNRs were performed on non-functionalized nanoribbons, as the bulky solubilizing groups can obscure imaging of fine structural details in GNRs and result in their on-surface self-assembly [6, 10, 15]. Therefore, for this study we developed a new synthetic approach for the non-functionalized GNRs that is illustrated by Fig. 1(a). Unlike other studies that used halogenated aromatic precursors for Ni⁰-mediated polymerization [4–7, 27, 32, 33, 41], we employed triflates as the leaving groups. We demonstrate that this approach yields high-quality nanoribbons and can likely be applied to the synthesis of other GNRs. The non-functionalized GNRs were deposited on InAs(110) substrate by the DCT approach and characterized by high-resolution STM/STS that confirmed the high structural quality of nanoribbons and revealed details of their electronic structure including energy states, electronic band gap and the spatial distribution of the local density of states. The experimental STS band gap of GNRs was found to be about 2 eV, which is very close to 2.35 eV predicted by the DFT simulations with GW correction, indicating a weak screening effect of InAs(110) substrate. Because of the reduced energy band gap of these ribbons, the GNR thin films exhibit appreciably high electrical conductivity and on/off ratios of about 10 in field-effect transistor measurements, suggesting their promise for device applications.

2 Results and discussion

The detailed description of the synthetic procedures for molecular precursor **1**, polymer **P1** and the final GNR is provided in the ESM along with the nuclear magnetic resonance (NMR), Fourier-transform infrared spectroscopy (FTIR) and matrix-assisted laser desorption/ionization (MALDI) mass spectrometry data. According to the results of size-exclusion chromatography measured with polystyrene standard, the weight average molecular weight of **P1** was ~ 36 kDa (see Fig. S4 in the ESM), corresponding to ~ 50 monomer units. According to this result, the length of these GNRs was comparable to that of laterally extended chevron GNRs, which were synthesized by the Ni⁰-mediated Yamamoto coupling using precursor molecules containing bromine rather than triflate leaving groups [7].

Raman spectroscopy is one of the standard techniques for characterization of GNRs. Raman spectra of GNRs depend on the energy of the excitation laser. For example, Raman spectra with sharp and well-resolved peaks could be recorded for $N = 7$ armchair GNRs [26], chevron [5] and laterally extended chevron GNRs [7] using a green excitation laser (532 nm, 2.33 eV). As discussed above, these GNRs have rather large and comparable band gaps ($\Delta^{\text{GW}} = 3.4\text{--}3.7$ eV; STS band gaps ~ 2.4–2.8 eV). On the contrary, for the GNRs with smaller band gaps, such as $N = 9$ armchair GNR ($\Delta^{\text{GW}} = 2.1$ eV; STS band gap ~ 1.4 eV), it is useful to also employ an infrared excitation laser (785 nm, 1.58 eV), which could resonantly excite the important radial-breathing-like mode (RBLM) [37]. The RBLM is not observed in Raman spectra of $N = 9$ armchair GNRs recorded with a green excitation laser [37].

As discussed in the Introduction, based on the results of GW calculations (Fig. 1(b)), the GNRs synthesized in this study have a comparable band gap to $N = 9$ armchair GNRs. Therefore, it could be expected that similar to the previous study [37], the 785 nm rather than 532 nm laser should resonantly excite the RBLM in these GNRs. Figure 1(c) shows Raman spectra of the GNRs synthesized in this study, which were recorded using four different excitation lasers: blue (405 nm, 3.06 eV), green (532 nm, 2.33 eV), red (633 nm, 1.96 eV) and infrared (785 nm, 1.58 eV). Indeed, the 785 nm infrared laser excites a low-wavenumber Raman mode at 198 cm⁻¹, which is barely visible in the spectrum recorded using the red laser and not observed in the spectra recorded using green and blue lasers.

Interestingly, while low-energy lasers enable low-wavenumber features in the Raman spectra of GNRs, high-wavenumber features are better seen in the spectra recorded using excitation lasers of higher energy. Figure 1(c) shows that the peaks at about 2,630, 2,920 and 3,200 cm⁻¹, which correspond to 2D, D+D' and 2D' modes, respectively, are not observed in the Raman spectrum recorded with the infrared laser and become more visible with the increase in the excitation laser energy. The effect of the laser energy on the Raman spectra of GNRs can also be illustrated by the D/G intensity ratio. The G band at 1,595 cm⁻¹ has higher energy than the D band at around 1,320 cm⁻¹, so the higher the energy of the excitation laser, the more intense the G band is relative to the D band. The dependence of the D/G intensity ratio on the excitation laser energy is shown in the inset in Fig. 1(c). Interestingly, while the spectral position of the G band does not depend on the laser energy, the D band exhibits such dependence, which is also shown in the inset in Fig. 1(c). Overall, since none of the lasers that we used efficiently excited both high- and low-energy vibrations of this GNR (Fig. 1(c)), these results demonstrate that it could be useful to employ several excitation lasers for Raman spectroscopy of graphene nanoribbons to reveal their spectroscopic features in a broad wavenumber range.

For the visualization of these GNRs by STM we used the DCT procedure [7, 30], which is illustrated by Fig. 2(a). A GNR powder was coated onto a fiberglass applicator and then brought into the chamber of a homebuilt STM system and annealed under UHV to remove residual solvent molecules and other adsorbates. Then, the applicator was pressed against a freshly cleaved InAs(110) substrate, and some of the ribbons were exfoliated from the GNR powder to the substrate's surface (Fig. 2(a)). For this study, we chose to use InAs(110) substrates for several reasons. InAs(110) is a well-known III-V semiconducting substrate, which has been studied both theoretically and experimentally [42, 43]. Its surface structure and electronic structure have been thoroughly investigated by STM and STS [44]. The electronic band gap of InAs(110) is

about 0.36 eV, which is much smaller than the predicted band gap of the GNRs synthesized in this work (Fig. 1(b)). The large difference in the band gaps of InAs(110) and nanoribbons facilitated the locating of the GNR band edges in the STS measurements. Unlike the InAs(111) surface, InAs(110) is non-polar, thus no significant charge transfer was expected [42, 45]. Theoretical work further predicts that only van der Waals forces are present between GNRs and the InAs(110) surface [46], so the interactions between the two are expected to be weak. At the same time, we were also confident that these weak interactions are still sufficiently strong to hold the GNRs in place for STM/STS characterization, as we found in our previous experiments on graphene nanoflakes [47] and carbon nanotubes [48] deposited on InAs(110).

Figure 2(b) is a filled-states STM topographic image taken at room temperature showing a GNR on the InAs(110) surface after DCT; the left end of this ribbon appears to overlap with another GNR that is likely three monomer units long. A small amount of debris from the DCT applicator was also deposited onto the surface but did not affect the characterization of the GNRs. The STM topograph shows the ribbon laying flat on the InAs(110) surface, which clearly exhibits arsenate dimer rows

spaced by 0.6 nm. The measured apparent height of the GNR is 0.3 nm (Fig. 2(c)), which is comparable to the previously reported values for graphene nanoflakes on InAs(110) [47] and chevron GNRs on hydrogen-passivated silicon, H:Si(100) [30]. Since the spacing between graphene layers in graphite is 0.34 nm, the 0.3 nm here indicates a possibly weak van der Waals interaction. The width of the GNR was measured to be 1.58 nm and the periodicity of the protrusions at the ribbon's edge is 1.34 nm (Fig. 2(c)); both values are very close to the expected geometrical parameters of this GNR (Fig. 1(a)). The high-resolution STM topographic images along with the dimensional profiles extracted from them confirm the expected geometry of the GNR.

While scanning in a constant-current mode with different parameters, we noticed that the GNRs showed different topographic appearances. This could be seen in the STM image shown in Fig. S5 in the ESM, which was obtained using a higher current. The image shows either a kinked GNR or touching termini of two GNRs and reveals the intra-ribbon structure. The paired protrusions shown on the GNRs' edges correspond to the two extra benzene rings at each elbow (Fig. 1(a)). The intra-ribbon structure represents not the graphene lattice but

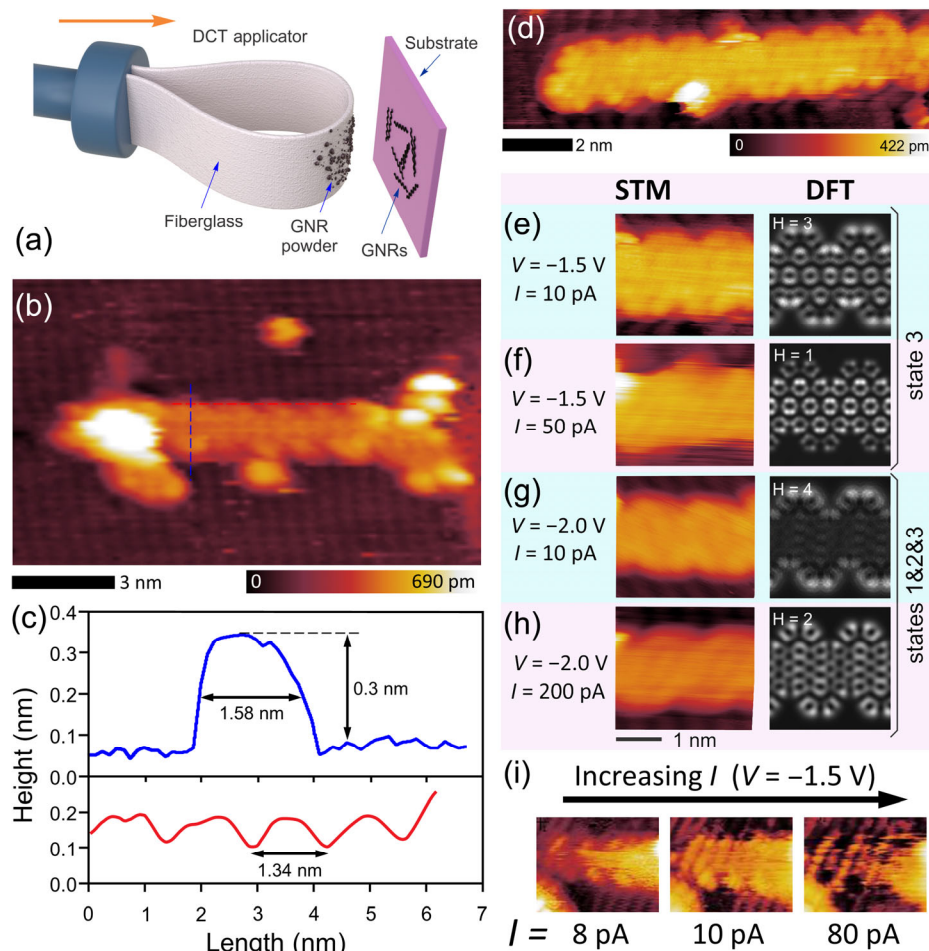


Figure 2 STM imaging of GNRs. (a) General scheme of DCT of GNRs on a STM substrate. (b) STM topographic image of a GNR on InAs(110) that was imaged with a sample bias of -2 V and tunneling current of 10 pA. (c) Height profiles measured across the GNR from panel (b) and along its edge. The positions of the height profiles are indicated in panel (b) by the dashed lines. (d) STM image of a GNR on InAs(110) scanned at a bias of -1.5 V and a tunneling current of 10 pA. (e)–(h) Fragments of the same GNR as in panel (d) scanned with the following parameters: (e) $V = -1.5$ V, $I = 10$ pA; (f) $V = -1.5$ V, $I = 50$ pA; (g) $V = -2.0$ V, $I = 10$ pA; (h) $V = -2.0$ V, $I = 200$ pA. Each STM image is complemented by the corresponding DFT-simulated LDOS map. In panels (e) and (f), the increase in the current (decrease in tip-ribbon distance) results in the disappearance of the GNR edge feature. The corresponding DFT-simulated LDOS maps for State 3 at the heights of 3 and 1 Å above the GNR show the same change in the topographic appearance of a ribbon. Likewise, in panels (g) and (h), the edge feature is better seen at a low tunneling current. The corresponding DFT-simulated LDOS maps for a mixture of States 1, 2 and 3 at the heights of 4 and 2 Å above the GNR predict a similar topographic change. (i) STM images of a fragment of the same ribbon taken at a constant bias of -1.5 V but with increasing current showing the tunable transparency of the GNR. The scans are 6 nm \times 5 nm.

the distribution of the local density of states (LDOS), which will be discussed in detail next. Figure 2(d) shows STM image of another GNR, a fragment of which was visualized using different imaging parameters (Figs. 2(e)–2(h)). By keeping the voltage constant but varying the tunneling current, we found a general trend as follows: as shown in Figs. 2(e), 2(f) and 2(g), and 2(h), when scanning with a lower current, that is, when the tip is further away from the GNR surface, the features at the GNR's edge appear brighter, clearer, and dominate over the features in the center. On the contrary, with a higher current, that is when scanning at a closer tip-GNR distance, the edge features start to disappear and those at the center start to emerge with clarity (Figs. 2(f) and 2(h)). The tunneling current depends on both the geometric structure and the electronic LDOS [49]. Since the geometry is invariant, the only thing that can change is the intensity of the LDOS at different heights above the ribbon. In other words, the spatial LDOS not only distributes inside the planar GNR, but also extends outward in the out-of-plane direction. This distribution in the z -direction can be treated as the energy states' decay length. For this GNR specifically, even though the states with different energies have different three-dimensional orbital shapes, the general trend is that the intensity of the LDOS of the edge states is weaker near the GNR surface, and decays slowly when further away from the surface; whereas the LDOS of the center states is stronger near the GNR surface, and decays fast outwards. Previous simulations on chevron GNRs also mentioned such changes in LDOS with different tip-sample distances [30], but no supporting experimental data were provided. Here we present STM images that capture such differences in the states' decay lengths. We also did DFT modeling of the LDOS maps at various heights above the GNR without the inclusion of the substrate (complete LDOS maps are shown in Fig. S6 in the ESM). After carefully determining the energy states by STS, we assigned the corresponding simulated LDOS maps for each case of Figs. 2(e)–2(h). These simulations are in very good agreement with the experimental results.

Previous simulation studies of GNRs on InAs(110) indicate that GNRs could show the tunable transparency effect [46], which was previously demonstrated for graphene nanoflakes on InAs [47]. Similarly, we found that GNRs on InAs(110) could be either transparent to the substrate's arsenate dimer rows or conceal them. With 52 images of GNRs on InAs(110) taken with different scanning parameters, we grouped them into three categories: (1) GNRs that are transparent to the substrate; (2) GNRs that are non-transparent with intra-ribbon resolution; and (3) GNRs that are non-transparent with no intra-ribbon resolution. Height statistics over these 52 images show that the average height for the 6 transparent GNRs is 0.21 nm, whereas for the 46 non-transparent ribbons with and without intra-ribbon lattice the average heights are 0.23 and 0.27 nm, respectively. The smaller apparent height for the transparent ribbons agrees with the results previously reported for graphene nanoflakes [47], indicating that GNRs were pushed towards the substrate and states from the substrate started to dominate the tunneling current and were "picked" up by the tip. This effect is illustrated by Fig. 2(i), which shows that the same GNR changes from non-transparent to transparent with increasing tunneling current. When scanned at -1.5 V and 8 pA, this GNR was non-transparent with an apparent height of 0.36 nm. When the current was changed to 10 pA, the tip moved closer to the surface and the GNR became partially transparent with the As dimer rows becoming visible and the ribbon's apparent height decreasing to 0.18 nm. With further current increase to 80 pA, the GNR appeared pushed to the substrate,

becoming completely transparent with an apparent height of only 0.12 nm. This transition from non-transparent to transparent with increasing current indicates that the InAs surface state decay length is shorter than that of GNRs, so the charge from the InAs dominates only at smaller distances. This makes InAs different from metal surfaces with larger state decay lengths, such as Cu(111) and Au(111). Away from the surface with a properly chosen tip-sample distance, the coupling between the InAs state and the GNR state is so weak that only the GNR state is probed by STM.

To determine the electronic structure of the GNR, we performed STS measurements. Figure 3(a) shows three normalized conductance (dI/dV) point spectra taken at the GNR edge (red curve), center (green curve) and on the InAs(110) substrate (blue curve), respectively. The spectrum on the InAs shows a band gap of 0.35 eV, which ensures the accuracy of the collected data. The point spectrum taken at the GNR edge shows six distinct peaks at -2.1 , -1.8 , -1.1 , 0.9 , 1.3 and 1.9 V, respectively, which we assign as States 1 through 6. For the spectrum taken at the center of the GNR, however, we see only five states, with a missing State 2. This indicates that State 2 is not located at the center of the GNR. Indeed, DFT simulations of State 2 (Fig. S6 in the ESM) confirmed that regardless of the distance from the GNR, State 2 has low LDOS at the center. The normalized dI/dV spectra map across the GNR is shown in Fig. 3(b) with three individual spectra marked by three dashed lines. Band edges for the GNRs and the substrate, as well as variations of the energy states are shown, e.g. State 2 disappears at the center of the GNR. The substrate conduction and valence band states also contribute to a small extent inside the GNR gap, but their intensities are rather weak. In order to verify the accuracy of the identified energy states, a DFT-simulated energy spectrum of an isolated GNR is shown in Fig. 3(c). Although DFT often underestimates GNR band gaps [34], other information including the energy states splitting, the spatial DOS mapping and the orbital shapes can be rather accurate [29]. The simulated energy splittings between State 1 and 2, 2 and 3, 4 and 5, 5 and 6 are 0.42, 0.65, 0.45, and 0.50 eV, respectively, which are consistent with the experimental STS data.

The peak-to-peak distance between States 3 and 4 in the normalized conductance spectrum (red and green curves in Fig. 3(a)) gives a band gap of about 2 eV for this GNR. To justify the consistency of the measured band gap, STS data were collected over 30 GNRs on InAs(110), and the averaged band gap was 2.03 eV. This value is very close to the GW band gap of 2.35 eV (Fig. 1(b)), which is only 0.35 eV larger than the experimentally determined value. Previous studies of chevron GNRs showed much larger differences between the theoretical GW and experimental STS band gaps due to screening effects from the substrates: $\Delta^{\text{GW}} - \Delta^{\text{STS}} \approx 0.9$ eV, when ribbons were measured on H:Si(100) [30], and $\Delta^{\text{GW}} - \Delta^{\text{STS}} \approx 1.2$ eV, when ribbons were measured on Au(111) [38–40]. Thus, compared to H:Si(100) and Au(111) substrates, surface states in InAs(110) seem to interfere less with the GNR band edge states, indicating a weaker substrate screening effect.

Following exfoliation onto the surface, we found the GNRs to be laying on the substrate with random orientations. Previously reported work for carbon nanotubes exfoliated onto InAs showed that the nanotubes have a preferential alignment to the InAs substrate due to formation of a weak chemical bond between the nanotube and substrate, and a change in nanotube electronic property was associated with changing substrate alignment [48]. We counted a total of 164 GNRs deposited on the surface and measured the angles between the

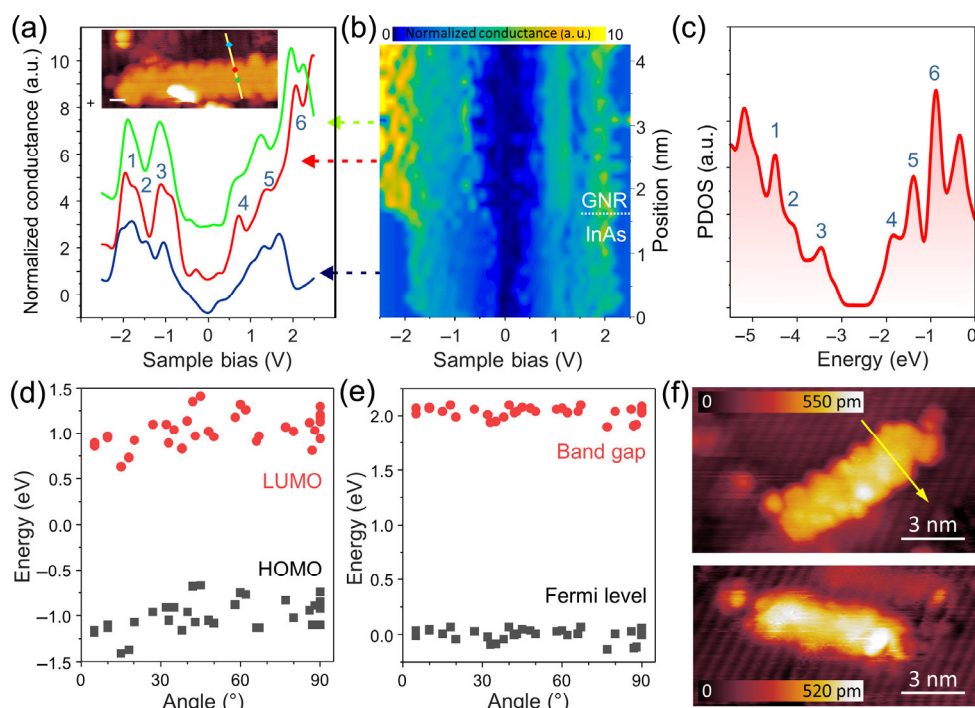


Figure 3 Scanning tunneling spectroscopy and nanomanipulation of GNRs on InAs(110). (a) Normalized tunneling conductance taken at the GNR edge (red), GNR center (green) and the substrate (blue) with six energy states identified. The inset shows a topographic image of the GNR on which the data were collected. Scale bar is 1 nm. (b) Normalized tunneling conductance spectra map along the GNR in the inset in panel (a). The blue, green, and red dashed lines indicate the positions of the spectra points shown in panel (a). The white dotted line indicates the point where the tip transitions from bare InAs(110) substrate to the GNR. (c) The projected density of states (PDOS) for an isolated GNR computed using DFT. Energy States 1 through 6 are marked at their corresponding peaks. (d) and (e) STS data collected over 30 GNRs with different alignments with respect to the InAs(110) substrate. Panel (d) shows HOMO and LUMO peaks of the 30 GNRs and panel (e) shows the corresponding band gaps and Fermi levels. The band gaps were found by calculating differences between the HOMO and LUMO energies and the Fermi levels were calculated by dividing the sums of HOMO and LUMO energies by 2. (f) Before and after images of a GNR manipulated by the STM tip; the yellow arrow indicates the motion of the tip. Scan parameters: -2 V, 10 pA.

ribbons and the InAs substrate: 0 degrees representing the GNR's longitudinal axis parallel to the As dimer row direction and 90 degrees representing the perpendicular case. From the histogram shown in Fig. S7 in the ESM, we observed that the GNRs were randomly distributed within the 10 subdivided intervals from 0 to 90 degrees, with no preferential registry. This indicates that no such chemical bond is present between the GNR and the InAs substrate. Figures 3(d) and 3(e) show graphs of STS data collected over 30 GNRs with different orientations, indicating the energies of the highest occupied molecular orbital (HOMO, State 3) and the lowest unoccupied molecular orbital (LUMO, State 4), band gaps and Fermi levels. The band gap for the GNRs with different orientations varies from 1.9 to 2.1 eV with an average value of 2.03 eV, a standard deviation of 0.05 eV. The Fermi level varies from -0.16 to 0.167 eV with an average value of 0.02 eV, a standard deviation of 0.17 eV (Fig. 3(e)). The narrow distributions of the band gap and the Fermi level position indicate no apparent change in the electronic structure for GNRs with different orientations. The slightly larger variation of the Fermi level could be caused by defects or contaminants on the surface. The mid-gap Fermi level suggests no significant charge transfer between the GNRs and the substrate. We also observed no length dependence of the GNR electronic structure in STS measurements of 30 GNRs with lengths ranging from a few nanometers to tens of nanometers.

The weak coupling between GNRs and InAs(110) enables nanomanipulation of ribbons using the STM tip. Figure 3(f) shows STM images of a GNR before and after the manipulation. The ribbon was rotated by about 60° by moving the tip along the direction indicated by the yellow arrow. The resolution

after manipulation deteriorated possibly due to deposition of contaminants on the tip. Because of the tip change, it was difficult to analyze the change in electronic structure before and after manipulation. However, Fig. S8 in the ESM gives an example of spectra maps taken before and after GNR manipulation with minimal tip change, showing no obvious change in the electronic structure after the manipulation.

The relatively low band gap of these GNRs compared to other ribbons from the chevron family [7, 22, 40] makes them promising for device measurements. Previously, these GNRs were synthesized with poly(ethylene oxide) (PEO) moieties [6] and were therefore well dispersible in common organic solvents, such as tetrahydrofuran (THF). A THF solution of PEO-functionalized GNRs could be drop-cast on a substrate with pre-fabricated Ti/Au electrodes, forming a conductive film upon THF evaporation that could be employed for electrical measurements [6]. The GNRs that we prepared in this study primarily for the STM characterization did not bear any solubilizing functional groups, so their solubility in common organic solvents was very poor [24]. Yet, these ribbons could be processed into uniform few-nm-thick films using the recently developed interfacial self-assembly approach [22]. In brief, the ribbons were first dissolved in chlorosulfonic acid (CSA), which is known as a very efficient solvent for graphitic materials [50, 51], and then a solution of GNRs in CSA was delivered to the surface of deionized (DI) water. Upon the reaction of CSA with water, the GNRs self-assembled on the water surface forming a densely packed film of π - π stacked nanoribbons [7, 22]. The GNR film was then washed by several consecutive transfers to the surface of DI water in other beakers and then fished out with a Si/SiO₂ substrate with pre-patterned gold

electrodes.

Figure 4(a) shows optical photograph of a typical GNR device fabricated in this study. Two $100\ \mu\text{m} \times 100\ \mu\text{m}$ Au electrodes on Si/SiO₂ are bridged by a GNR film, which covers the entire substrate. Figure 4(b) shows an optical photograph of another area of the substrate with a crack in the GNR film formed during the manual transfer, which could be used for the atomic force microscopy (AFM) analysis. An AFM image of the area indicated by the blue square in Fig. 4(b) is shown in Fig. 4(c). Outside of the crack area the ribbons are densely packed, and the film exhibits only occasional pinholes. Figure 4(d) shows the AFM height profile measured along the red line in Fig. 4(c). As we discussed in detail in our previous works, in the described approach the ribbons self-assemble in the edge-on geometry—as the films form on a surface of water, the GNRs in such geometry minimize their area of interaction with the hydrophilic interface and engage in π - π interactions with other ribbons [7, 22]. Thus, the measured film thickness of $\sim 4\ \text{nm}$ (Fig. 4(d)) may correspond to two monolayers of GNRs standing on their edges. AFM measurements performed on other cracked regions of the same film yielded comparable thickness values. This self-assembly approach therefore enables fabrication of very thin and uniform films of GNRs on a large scale.

Despite their small thickness, the GNR devices were electrically conductive as shown in Fig. 4(e). In these measurements, the $100\ \mu\text{m} \times 100\ \mu\text{m}$ Au pads served as source (S) and drain (D) electrodes and the heavily p-doped silicon, which was separated from the pads and the GNR film by the 300 nm thick layer of SiO₂, served as a global gate (G) electrode. We produced GNR devices with 2 and 4 μm gaps between $100\ \mu\text{m} \times 100\ \mu\text{m}$ Au electrodes, and all of them exhibited similar drain-source current (I_{DS})–gate voltage (V_{G}) dependencies as shown in Fig. 4(e). Compared to the chevron GNR films that we characterized previously in similar measurements [22], these GNRs were much more conductive, which was expected due to their smaller band gap. They also showed a p-type behavior, but unlike the $I_{\text{DS}}-V_{\text{G}}$ dependencies for the chevron GNR films, which exhibited monotonous I_{DS} decay in the entire V_{G} range [22], these GNRs exhibit a minimum around $V_{\text{G}} = 0$ and then a slight I_{DS} increase at positive gate voltages,

indicating some electronic conductivity. The devices exhibited on-off current ratios ranging from 5 to 12 (Fig. 4(e)), which are some of the highest values reported for bulk measurements of solution-processed GNRs. All devices showed linear $I_{\text{DS}}-V_{\text{G}}$ dependencies, as illustrated by the inset in Fig. 4(e). Since these measurements were performed on GNR thin films, they probe not only the intrinsic properties of nanoribbons but also multiple inter-GNR junctions. Yet, the reasonably high currents obtained even at $V_{\text{DS}} = 1\ \text{V}$, well-developed and reproducible transfer characteristics and on-off ratios of about 10 already observed in a bulk form (Fig. 4(e)) suggest that single-GNR measurements [35] performed on these ribbons could reveal competitive electronic properties for the GNR field.

3 Conclusions

In summary, we report solution synthesis and detailed STM/STS characterization of atomically precise GNRs with a meandering shape that are structurally related to chevron GNRs but have a reduced energy band gap. The ribbons were synthesized by Ni⁰-mediated Yamamoto polymerization of specially designed molecular precursors using triflates as the leaving groups and oxidative cyclodehydrogenation of the resulting polymers using Scholl reaction. The ribbons were deposited onto III-V semiconducting InAs(110) substrates by a dry contact transfer technique. High-resolution STM/STS characterization not only confirmed the GNR geometry, but also revealed details of electronic structure including energy states, electronic band gap, as well as the spatial distribution of the local density of states. The experimental STS band gap of GNRs is about 2 eV, which is very close to 2.35 eV predicted by the GW simulations indicating a weak screening effect of InAs(110) substrate. Furthermore, several aspects of GNR-InAs(110) substrate interactions were also probed and analyzed, including GNR tunable transparency, alignment to the substrate, and manipulations of GNR position by the STM tip. The weak interaction between the GNRs and the InAs(110) surface makes InAs(110) an ideal substrate for investigating the intrinsic properties of GNRs. Because of the reduced energy band gap of these ribbons, the GNR thin films exhibit appreciably high electrical conductivity and on/off ratios of about 10 in field-

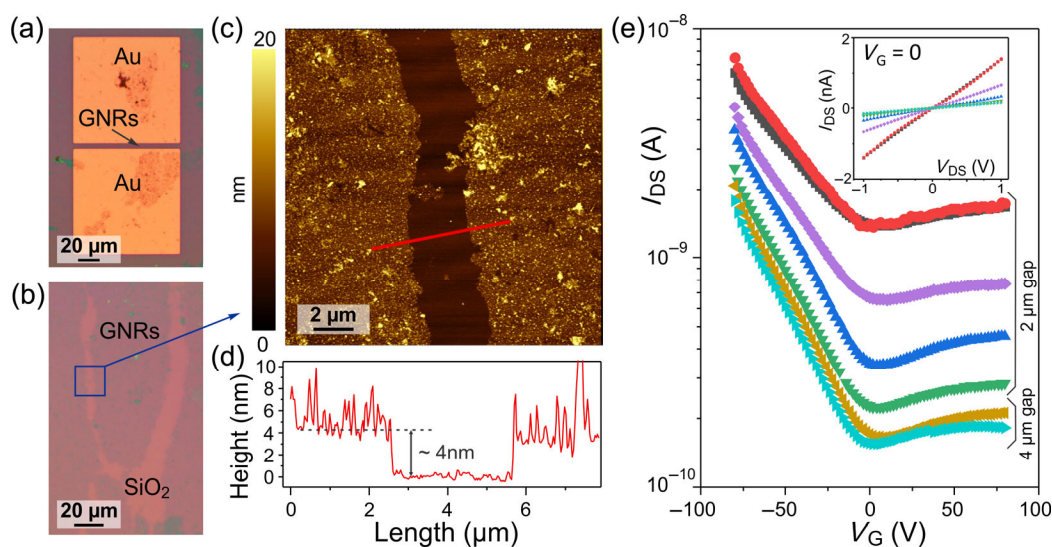


Figure 4 Electrical characterization of GNRs. (a) Optical photograph of a representative device, in which a GNR film covers a Si/SiO₂ substrate with square Au contacts. (b) A photograph showing optical contrast between the GNR film and bare Si/SiO₂ substrate in the area where the film formed cracks during the manual transfer. (c) AFM image of the area of the GNR-covered Si/SiO₂ substrate shown by the blue square in panel (b). (d) AFM height profile measured along the red line in panel (c). (e) $I_{\text{DS}}-V_{\text{G}}$ dependencies measured for several GNR devices with 2 and 4 μm gaps between gold electrodes; $V_{\text{DS}} = 1\ \text{V}$. $I_{\text{DS}}-V_{\text{DS}}$ dependencies for the same devices measured at $V_{\text{G}} = 0$ are shown in the inset.

effect transistor measurements, suggesting their promise for device applications.

4 Experimental

4.1 Synthesis and characterization of GNRs

The details of the synthesis of GNRs along with the corresponding NMR, FTIR and mass spectrometry data are provided in the ESM. Raman spectroscopy was performed using a Horiba LabRAM HR Evolution Raman microscope with 405, 532, 633 and 785 nm excitation lasers.

4.2 STM characterization

Cross-sectional STM imaging of InAs(110) and GNRs was conducted using a home-built Lyding-style STM [52] operating in ultra-high vacuum (base pressure 5×10^{-11} Torr) at room temperature. A constant-current scanning mode was used throughout the experiment with various sample biases and tunneling currents. InAs(110) was prepared by mounting the InAs vertically with its cross section facing toward tip. InAs samples were degassed at around 120 °C for 8–16 h, then a thin layer of titanium was evaporated onto the sample *in situ* to serve as a getter for contaminants. The InAs(110) sample was then cleaved *in situ*, exposing a clean (110) surface with the 1×1 surface relaxation. The InAs wafers used were p-type Zn-doped with a sheet resistance of 5–20 m Ω -cm. Field-directed sputter sharpened tungsten probes from Tiptek and chemically etched tungsten tips were used for collecting STS and STM data. The DCT applicator was prepared by coating a piece of fiberglass with the GNR powder. The applicator was translated into UHV and degassed at elevated temperatures until the pressure reached the base pressure. GNRs were then exfoliated onto the InAs surface by pressing the GNR coated fiberglass applicator against the cleaved surface. STS data were collected in variable-spacing mode ($dS = -2$ Å) to further eliminate electronic noise. The data were then corrected by an exponential factor to account for the change in current due to movement of the tip [53]. GNR manipulation was performed by moving the tip at 80 Å·s⁻¹ with a sample bias of -2 V and a tunneling current of 0.2 nA.

4.3 Device fabrication and electrical measurements

Square 100 $\mu\text{m} \times 100 \mu\text{m}$ Au electrodes separated by 2 or 4 μm gaps were fabricated on heavily p-doped Si substrates covered with a 300 nm thick layer of SiO₂ by standard electron-beam lithography using a Zeiss Supra 40 field-emission scanning electron microscope and a Raith pattern generator. The electron beam deposition of metal contacts was performed using an AJA electron beam evaporation system. We first deposited 3 nm of Cr, which served as an adhesion layer for gold contacts, and then 12 nm of Au. The GNR films were prepared from a CSA solution using the interfacial self-assembly approach as described in our previous work [7, 22]. The films were transferred to Si/SiO₂ substrates with prefabricated Au electrodes and imaged by AFM using a Digital Instruments Nanoscope IIIa Dimension 3100 system. Similar to the previous study [6], we also annealed the GNR devices in Ar/H₂ at 500 °C to remove solvent residues and other adsorbates and improve the devices contacts.

The electrical measurements of GNR devices were performed using an Agilent 4155C semiconductor parameter analyzer. The measurements were performed in a Lake Shore TTPX cryogenic probe station at the base pressure of about 2×10^{-6} Torr. The devices were evacuated for at least 2 days before the measurements to minimize the effect of surface adsorbates [54].

4.4 DFT simulations

The calculations of projected density of states (PDOS) and local density of states (LDOS) for the infinite GNR were conducted by QUANTUM ESPRESSO package [55], with a supercell periodic in the GNR axis direction and large enough in the other two directions to separate the GNR and its images. Norm-conserving pseudopotentials with the Becke-Lee-Yang-Parr (BLYP) exchange-correlation functional [56] were used with a 60 Ry plane-wave energy cutoff. A Monkhorst-Pack grid of $2 \times 1 \times 1$ was used for structural relaxations and $16 \times 1 \times 1$ for electronic property calculations. The structure was optimized until the maximum residual force was less than 0.02 eV·Å⁻¹. Based on the PDOS, three states above and three states below the Fermi level at the corresponding peaks were captured, followed by the LDOS calculations. The LDOS for these six states were calculated at the planes located 1–4 Å above the GNR. The visualizations of GNR geometry and LDOS were performed with XCrysDen software [57].

The DFT band structure for the infinite GNR with periodic boundary condition was calculated with SIESTA software [58]. We employed generalized gradient approximation (GGA) with Perdew-Burke-Ernzerhof (PBE) exchange-correlation functional [59]. The double zeta polarized basis set (DZP) was used with a mesh cutoff of 300 Ry. A Monkhorst-Pack grid of $2 \times 1 \times 1$ was used for structural relaxation and $18 \times 1 \times 1$ for band structure calculation.

The GW band structure calculation for the infinite GNR was performed by VASP package with the PBE exchange-correlation functional [60]. The projected augmented wave (PAW) pseudopotentials with a 400 eV energy cutoff were employed. The Gamma-point-centered *k*-grids of $4 \times 1 \times 1$ was applied. The ground state was obtained by performing DFT simulations first. Then the quasi-particle energies were calculated with the single-shot G0W0 approximation in VASP [61]. The parameter settings were similar to our previous work [30]. Since this GNR has large band dispersions, the Wannier interpolation was performed to obtain the G0W0 bands using WANNIER90 package [62].

Acknowledgements

The work was supported by the Office of Naval Research (No. N00014-19-1-2596) and the National Science Foundation (NSF) through CHE-1455330. Some experiments were performed with the support of Nebraska Materials Research Science and Engineering Center (NSF DMR-1420645) using the instrumentation at Nebraska Nanoscale Facility, which is supported by the NSF (ECCS-1542182) and the Nebraska Research Initiative. All the simulations were performed on the Blue Water computation resources provided by the University of Illinois at Urbana-Champaign.

Electronic Supplementary Material: Supplementary material (detailed synthesis of GNRs along with the corresponding NMR, FTIR, mass spectrometry and SEC data, additional STM and STS data, DFT-simulated LDOS maps of GNR calculated at different tip-ribbon distances, nanomanipulation of a GNR on InAs(110) using an STM tip) is available in the online version of this article at <https://doi.org/10.1007/s12274-020-2797-6>.

References

- [1] Nakada, K.; Fujita, M.; Dresselhaus, G.; Dresselhaus, M. S. Edge state in graphene ribbons: Nanometer size effect and edge shape dependence. *Phys. Rev. B* **1996**, *54*, 17954–17961.
- [2] Yang, L.; Park, C. H.; Son, Y. W.; Cohen, M. L.; Louie, S. G.

- Quasiparticle energies and band gaps in graphene nanoribbons. *Phys. Rev. Lett.* **2007**, *99*, 186801.
- [3] Barone, V.; Hod, O.; Scuseria, G. E. Electronic structure and stability of semiconducting graphene nanoribbons. *Nano Lett.* **2006**, *6*, 2748–2754.
- [4] Schwab, M. G.; Narita, A.; Hernandez, Y.; Balandina, T.; Mali, K. S.; De Feyter, S.; Feng, X. L.; Müllen, K. Structurally defined graphene nanoribbons with high lateral extension. *J. Am. Chem. Soc.* **2012**, *134*, 18169–18172.
- [5] Vo, T. H.; Shekhirev, M.; Kunkel, D. A.; Morton, M. D.; Berglund, E.; Kong, L. M.; Wilson, P. M.; Dowben, P. A.; Enders, A.; Sinitskii, A. Large-scale solution synthesis of narrow graphene nanoribbons. *Nat. Commun.* **2014**, *5*, 3189.
- [6] Huang, Y. J.; Mai, Y. Y.; Beser, U.; Teyssandier, J.; Velpula, G.; van Gorp, H.; Straasø, L. A.; Hansen, M. R.; Rizzo, D.; Casiraghi, C. et al. Poly(ethylene oxide) functionalized graphene nanoribbons with excellent solution processability. *J. Am. Chem. Soc.* **2016**, *138*, 10136–10139.
- [7] Mehdi Pour, M.; Lashkov, A.; Radocea, A.; Liu, X. M.; Sun, T.; Lipatov, A.; Korlacki, R. A.; Shekhirev, M.; Aluru, N. R.; Lyding, J. W. et al. Laterally extended atomically precise graphene nanoribbons with improved electrical conductivity for efficient gas sensing. *Nat. Commun.* **2017**, *8*, 820.
- [8] Yang, X. Y.; Dou, X.; Rouhanipour, A.; Zhi, L. J.; Räder, H. J.; Müllen, K. Two-dimensional graphene nanoribbons. *J. Am. Chem. Soc.* **2008**, *130*, 4216–4217.
- [9] Yang, W. L.; Lucotti, A.; Tommasini, M.; Chalifoux, W. A. Bottom-up synthesis of soluble and narrow graphene nanoribbons using alkyne benzannulations. *J. Am. Chem. Soc.* **2016**, *138*, 9137–9144.
- [10] Li, G.; Yoon, K. Y.; Zhong, X. J.; Zhu, X. Y.; Dong, G. B. Efficient bottom-up preparation of graphene nanoribbons by mild Suzuki–Miyaura polymerization of simple triaryl monomers. *Chem.—Eur. J.* **2016**, *22*, 9116–9120.
- [11] Li, G.; Yoon, K. Y.; Zhong, X. J.; Wang, J. C.; Zhang, R.; Guest, J. R.; Wen, J. G.; Zhu, X. Y.; Dong, G. B. A modular synthetic approach for band-gap engineering of armchair graphene nanoribbons. *Nat. Commun.* **2018**, *9*, 1687.
- [12] Kim, K. T.; Jung, J. W.; Jo, W. H. Synthesis of graphene nanoribbons with various widths and its application to thin-film transistor. *Carbon* **2013**, *63*, 202–209.
- [13] Daigle, M.; Miao, D. D.; Lucotti, A.; Tommasini, M.; Morin, J. F. Helically coiled graphene nanoribbons. *Angew. Chem., Int. Ed.* **2017**, *56*, 6213–6217.
- [14] Fogel, Y.; Zhi, L. J.; Rouhanipour, A.; Andrienko, D.; Räder, H. J.; Müllen, K. Graphitic nanoribbons with dibenzo[*e*, *l*]pyrene repeat units: Synthesis and self-assembly. *Macromolecules* **2009**, *42*, 6878–6884.
- [15] Narita, A.; Feng, X. L.; Hernandez, Y.; Jensen, S. A.; Bonn, M.; Yang, H. F.; Verzhbitskiy, I. A.; Casiraghi, C.; Hansen, M. R.; Koch, A. H. R. et al. Synthesis of structurally well-defined and liquid-phase-processable graphene nanoribbons. *Nat. Chem.* **2014**, *6*, 126–132.
- [16] Narita, A.; Verzhbitskiy, I. A.; Frederickx, W.; Mali, K. S.; Jensen, S. A.; Hansen, M. R.; Bonn, M.; De Feyter, S.; Casiraghi, C.; Feng, X. L. et al. Bottom-up synthesis of liquid-phase-processable graphene nanoribbons with near-infrared absorption. *ACS Nano* **2014**, *8*, 11622–11630.
- [17] Hu, Y. B.; Xie, P.; De Corato, M.; Ruini, A.; Zhao, S.; Meggendorfer, F.; Straasø, L. A.; Rondin, L.; Simon, P.; Li, J. et al. Bandgap engineering of graphene nanoribbons by control over structural distortion. *J. Am. Chem. Soc.* **2018**, *140*, 7803–7809.
- [18] Narita, A.; Wang, X. Y.; Feng, X. L.; Müllen, K. New advances in nanographene chemistry. *Chem. Soc. Rev.* **2015**, *44*, 6616–6643.
- [19] Shekhirev, M.; Sinitskii, A., Solution synthesis of atomically precise graphene nanoribbons. In *Chemistry of Carbon Nanostructures*. Müllen, K.; Feng, X., Eds.; De Gruyter: Berlin, 2017; pp 194–225.
- [20] Abbas, A. N.; Liu, G.; Narita, A.; Orosco, M.; Feng, X. L.; Müllen, K.; Zhou, C. W. Deposition, characterization, and thin-film-based chemical sensing of ultra-long chemically synthesized graphene nanoribbons. *J. Am. Chem. Soc.* **2014**, *136*, 7555–7558.
- [21] Gao, J.; Uribe-Romo, F. J.; Saathoff, J. D.; Arslan, H.; Crick, C. R.; Hein, S. J.; Itin, B.; Clancy, P.; Dichtel, W. R.; Loo, Y. L. Ambipolar transport in solution-synthesized graphene nanoribbons. *ACS Nano* **2016**, *10*, 4847–4856.
- [22] Shekhirev, M.; Vo, T. H.; Mehdi Pour, M.; Lipatov, A.; Munukutla, S.; Lyding, J. W.; Sinitskii, A. Interfacial self-assembly of atomically precise graphene nanoribbons into uniform thin films for electronics applications. *ACS Appl. Mater. Interfaces* **2017**, *9*, 693–700.
- [23] Zschiechang, U.; Klauk, H.; Müeller, I. B.; Strudwick, A. J.; Hentermann, T.; Schwab, M. G.; Narita, A.; Feng, X. L.; Müllen, K.; Weitz, R. T. Electrical characteristics of field-effect transistors based on chemically synthesized graphene nanoribbons. *Adv. Electron. Mater.* **2015**, *1*, 1400010.
- [24] Shekhirev, M.; Vo, T. H.; Kunkel, D. A.; Lipatov, A.; Enders, A.; Sinitskii, A. Aggregation of atomically precise graphene nanoribbons. *RSC Adv.* **2017**, *7*, 54491–54499.
- [25] Konnerth, R.; Cervetti, C.; Narita, A.; Feng, X.; Müllen, K.; Hoyer, A.; Burghard, M.; Kern, K.; Dressel, M.; Bogani, L. Tuning the deposition of molecular graphene nanoribbons by surface functionalization. *Nanoscale* **2015**, *7*, 12807–12811.
- [26] Cai, J. M.; Ruffieux, P.; Jaafar, R.; Bieri, M.; Braun, T.; Blankenburg, S.; Muoth, M.; Seitsonen, A. P.; Saleh, M.; Feng, X. L. et al. Atomically precise bottom-up fabrication of graphene nanoribbons. *Nature* **2010**, *466*, 470–473.
- [27] Vo, T. H.; Perera, U. G. E.; Shekhirev, M.; Mehdi Pour, M.; Kunkel, D. A.; Lu, H. D.; Gruverman, A.; Sutter, E.; Cotlet, M.; Nykypanchuk, D. et al. Nitrogen-doping induced self-assembly of graphene nanoribbon-based two-dimensional and three-dimensional metamaterials. *Nano Lett.* **2015**, *15*, 5770–5777.
- [28] Wang, S. D.; Wang, J. L. Quasiparticle energies and optical excitations in chevron-type graphene nanoribbon. *J. Phys. Chem. C* **2012**, *116*, 10193–10197.
- [29] Liang, L. B.; Meunier, V. Electronic structure of assembled graphene nanoribbons: Substrate and many-body effects. *Phys. Rev. B* **2012**, *86*, 195404.
- [30] Radocea, A.; Sun, T.; Vo, T. H.; Sinitskii, A.; Aluru, N. R.; Lyding, J. W. Solution-synthesized chevron graphene nanoribbons exfoliated onto H:Si(100). *Nano Lett.* **2017**, *17*, 170–178.
- [31] Teeter, J. D.; Zahl, P.; Mehdi Pour, M.; Costa, P. S.; Enders, A.; Sinitskii, A. On-surface synthesis and spectroscopic characterization of laterally extended chevron graphene nanoribbons. *ChemPhysChem* **2019**, *20*, 2281–2285.
- [32] Huang, Y. J.; Xu, F. G.; Ganzer, L.; Camargo, F. V. A.; Nagahara, T.; Teyssandier, J.; van Gorp, H.; Basse, K.; Straasø, L. A.; Nagyte, V. et al. Intrinsic properties of single graphene nanoribbons in solution: Synthetic and spectroscopic studies. *J. Am. Chem. Soc.* **2018**, *140*, 10416–10420.
- [33] Huang, Y. J.; Dou, W. T.; Xu, F. G.; Ru, H. B.; Gong, Q. Y.; Wu, D. Q.; Yan, D. Y.; Tian, H.; He, X. P.; Mai, Y. Y. et al. Supramolecular nanostructures of structurally defined graphene nanoribbons in the aqueous phase. *Angew. Chem., Int. Ed.* **2018**, *57*, 3366–3371.
- [34] Ruffieux, P.; Cai, J. M.; Plumb, N. C.; Patthey, L.; Prezzi, D.; Ferretti, A.; Molinari, E.; Feng, X. L.; Müllen, K.; Pignedoli, C. A. et al. Electronic structure of atomically precise graphene nanoribbons. *ACS Nano* **2012**, *6*, 6930–6935.
- [35] Llinas, J. P.; Fairbrother, A.; Borin Barin, G.; Shi, W.; Lee, K.; Wu, S.; Yong Choi, B.; Braganza, R.; Lear, J.; Kau, N. et al. Short-channel field-effect transistors with 9-atom and 13-atom wide graphene nanoribbons. *Nat. Commun.* **2017**, *8*, 633.
- [36] Chen, Y. C.; de Oteyza, D. G.; Pedramrazi, Z.; Chen, C.; Fischer, F. R.; Crommie, M. F. Tuning the band gap of graphene nanoribbons synthesized from molecular precursors. *ACS Nano* **2013**, *7*, 6123–6128.
- [37] Talirz, L.; Söde, H.; Dumsloff, T.; Wang, S. Y.; Sanchez-Valencia, J. R.; Liu, J.; Shinde, P.; Pignedoli, C. A.; Liang, L. B.; Meunier, V. et al. On-surface synthesis and characterization of 9-atom wide armchair graphene nanoribbons. *ACS Nano* **2017**, *11*, 1380–1388.
- [38] Nguyen, G. D.; Tsai, H. Z.; Omrani, A. A.; Marangoni, T.; Wu, M.; Rizzo, D. J.; Rodgers, G. F.; Cloke, R. R.; Durr, R. A.; Sakai, Y. et al. Atomically precise graphene nanoribbon heterojunctions from a single molecular precursor. *Nat. Nanotechnol.* **2017**, *12*, 1077–1082.
- [39] Deniz, O.; Sánchez-Sánchez, C.; Jaafar, R.; Khariche, N.; Liang, L.; Meunier, V.; Feng, X.; Müllen, K.; Fasel, R.; Ruffieux, P. Electronic characterization of silicon intercalated chevron graphene nanoribbons on Au(111). *Chem. Commun.* **2018**, *54*, 1619–1622.
- [40] Shekhirev, M.; Zahl, P.; Sinitskii, A. Phenyl functionalization of

- atomically precise graphene nanoribbons for engineering inter-ribbon interactions and graphene nanopores. *ACS Nano* **2018**, *12*, 8662–8669.
- [41] Vo, T. H.; Shekirev, M.; Kunkel, D. A.; Orange, F.; Guinel, M. J. F.; Enders, A.; Sinitskii, A. Bottom-up solution synthesis of narrow nitrogen-doped graphene nanoribbons. *Chem. Commun.* **2014**, *50*, 4172–4174.
- [42] Szamota-Leandersson, K. Electronic structure of clean and adsorbate-covered InAs surfaces. Ph.D. Dissertation, Royal Institute of Technology, Sweden, 2010.
- [43] Andersson, C. B. M.; Andersen, J. N.; Persson, P. E. S.; Karlsson, U. O. Surface electronic structure of InAs(110). *Phys. Rev. B* **1993**, *47*, 2427–2430.
- [44] Klijn, J.; Sacharow, L.; Meyer, C.; Blügel, S.; Morgenstern, M.; Wiesendanger, R. Stm measurements on the InAs(110) surface directly compared with surface electronic structure calculations. *Phys. Rev. B* **2003**, *68*, 205327.
- [45] Yélgel, C.; Srivastava, G. P.; Miwa, R. H. *Ab initio* investigation of the electronic properties of graphene on InAs(111)A. *J. Phys. Condens. Matter* **2012**, *24*, 485004.
- [46] Andrade, D. P.; Miwa, R. H.; Srivastava, G. P. Graphene and graphene nanoribbons on InAs(110) and Au/InAs(110) surfaces: An *ab initio* study. *Phys. Rev. B* **2011**, *84*, 165322.
- [47] He, K. T.; Koepke, J. C.; Barraza-Lopez, S.; Lyding, J. W. Separation-dependent electronic transparency of monolayer graphene membranes on III–V semiconductor substrates. *Nano Lett.* **2010**, *10*, 3446–3452.
- [48] Ruppalt, L. B.; Lyding, J. W. Charge transfer between semiconducting carbon nanotubes and their doped GaAs(110) and InAs(110) substrates detected by scanning tunnelling spectroscopy. *Nanotechnology* **2007**, *18*, 215202.
- [49] Tersoff, J.; Hamann, D. R. Theory of the scanning tunneling microscope. *Phys. Rev. B* **1985**, *31*, 805–813.
- [50] Davis, V. A.; Parra-Vasquez, A. N. G.; Green, M. J.; Rai, P. K.; Behabtu, N.; Prieto, V.; Booker, R. D.; Schmidt, J.; Kesselman, E.; Zhou, W. et al. True solutions of single-walled carbon nanotubes for assembly into macroscopic materials. *Nat. Nanotechnol.* **2009**, *4*, 830–834.
- [51] Behabtu, N.; Lomeda, J. R.; Green, M. J.; Higginbotham, A. L.; Sinitskii, A.; Kosynkin, D. V.; Tsentlovich, D.; Parra-Vasquez, A. N. G.; Schmidt, J.; Kesselman, E. et al. Spontaneous high-concentration dispersions and liquid crystals of graphene. *Nat. Nanotechnol.* **2010**, *5*, 406–411.
- [52] Lyding, J. W.; Skala, S.; Hubacek, J. S.; Brockenbrough, R.; Gammie, G. Variable-temperature scanning tunneling microscope. *Rev. Sci. Instrum.* **1988**, *59*, 1897–1902.
- [53] Ruppalt, L. B.; Lyding, J. W. Metal-induced gap states at a carbon-nanotube intramolecular heterojunction observed by scanning tunneling microscopy. *Small* **2007**, *3*, 280–284.
- [54] Sinitskii, A.; Dimiev, A.; Kosynkin, D. V.; Tour, J. M. Graphene nanoribbon devices produced by oxidative unzipping of carbon nanotubes. *ACS Nano* **2010**, *4*, 5405–5413.
- [55] Giannozzi, P.; Baroni, S.; Bonini, N.; Calandra, M.; Car, R.; Cavazzoni, C.; Ceresoli, D.; Chiarotti, G. L.; Cococcioni, M.; Dabo, I. et al. QUANTUM ESPRESSO: A modular and open-source software project for quantum simulations of materials. *J. Phys. Condens. Matter* **2009**, *21*, 395502.
- [56] Becke, A. D. Density-functional exchange-energy approximation with correct asymptotic behavior. *Phys. Rev. A* **1988**, *38*, 3098–3100.
- [57] Kokalj, A. XCrySDen—a new program for displaying crystalline structures and electron densities. *J. Mol. Graph. Model.* **1999**, *17*, 176–179.
- [58] Soler, J. M.; Artacho, E.; Gale, J. D.; García, A.; Junquera, J.; Ordejón, P.; Sánchez-Portal, D. The SIESTA method for *ab initio* order-*N* materials simulation. *J. Phys. Condens. Matter* **2002**, *14*, 2745–2779.
- [59] Perdew, J. P.; Burke, K.; Ernzerhof, M. Generalized gradient approximation made simple. *Phys. Rev. Lett.* **1996**, *77*, 3865–3868.
- [60] Kresse, G.; Furthmüller, J. Efficient iterative schemes for *ab initio* total-energy calculations using a plane-wave basis set. *Phys. Rev. B* **1996**, *54*, 11169–11186.
- [61] Shishkin, M.; Kresse, G. Self-consistent *GW* calculations for semiconductors and insulators. *Phys. Rev. B* **2007**, *75*, 235102.
- [62] Mostofi, A. A.; Yates, J. R.; Lee, Y. S.; Souza, I.; Vanderbilt, D.; Marzari, N. Wannier90: A tool for obtaining maximally-localised wannier functions. *Comput. Phys. Commun.* **2008**, *178*, 685–699.